Simultaneous all-optical manipulation and recording of neural circuit activity with cellular resolution *in vivo*

Adam M Packer[1,2], Lloyd E Russell[1,2], Henry W P Dalgleish[1,2] & Michael Häusser[1,2]

We describe an all-optical strategy for simultaneously manipulating and recording the activity of multiple neurons with cellular resolution *in vivo*. We performed simultaneous two-photon optogenetic activation and calcium imaging by coexpression of a red-shifted opsin and a genetically encoded calcium indicator. A spatial light modulator allows tens of user-selected neurons to be targeted for spatiotemporally precise concurrent optogenetic activation, while simultaneous fast calcium imaging provides high-resolution network-wide readout of the manipulation with negligible optical cross-talk. Proof-of-principle experiments in mouse barrel cortex demonstrate interrogation of the same neuronal population during different behavioral states and targeting of neuronal ensembles based on their functional signature. This approach extends the optogenetic toolkit beyond the specificity obtained with genetic or viral approaches, enabling high-throughput, flexible and long-term optical interrogation of functionally defined neural circuits with single-cell and single-spike resolution in the mouse brain *in vivo*.

Optogenetic actuators are rapidly revolutionizing experimental manipulations of neural activity, enabling activation and inactivation with millisecond precision at the spatial scale of populations of neurons[1], and calcium indicators of activity in neurons now permit quantitative readout of neural activity from hundreds of neurons with cellular resolution[2]. A combination of these two experimental approaches is highly desirable for manipulating and recording the activity of many neurons simultaneously at the spatial and temporal resolution at which they function *in vivo* (**Fig. 1a**). Two-photon excitation provides the optical sectioning and signal-to-noise ratio required to achieve such a goal with single-cell and single-spike precision in both the imaging and the stimulation channels. However, two-photon calcium imaging and two-photon optogenetics have yet to be combined effectively (but see ref. 3). Moreover, the ability to individually target multiple neurons concurrently with patterned photostimulation is crucial for generating and manipulating natural patterns of activity *in vivo*.

Previous implementations of simultaneous manipulation and readout of neural activity are associated with a range of limitations, including manipulation artifacts on the recording channel, inadvertent activation caused by the recording and lack of spatial resolution. Purely electrophysiological approaches suffer from electrical artifacts in the recording channel during stimulation, the inherent invasiveness of the recordings and the inability to target large groups of neurons while maintaining single-cell resolution. Optical approaches have so far suffered from similar drawbacks. One-photon actuation not only stimulates many cells simultaneously (even when purposefully minimized[4]), but also can generate a large optical artifact in the imaging channel due to spectral overlap of the actuator excitation and readout emission wavelengths. This results in data loss during the crucial photostimulation period, as either the imaging sensor must be blanked or data must be discarded[5–7]. Promising approaches to differentiate the manipulation and recording wavelengths have been employed in *Caenorhabditis elegans*, although not with single-action-potential resolution[8]. Additionally, one-photon widefield excitation generates optical artifacts due to substantial autofluorescence throughout the tissue and does not permit targetable manipulations with cellular resolution. Simultaneous two-photon holographic imaging and photostimulation methods relying on glutamate uncaging have been employed only *in vitro*[9,10]. Combined optical and electrophysiological approaches also show promise for specific applications[11–13], although it can be difficult to ascertain which neurons are being directly activated and which are downstream of the activated neurons[14,15].

Here, we took advantage of the superior optical sectioning afforded by *in vivo* two-photon microscopy[16,17] to precisely activate multiple identified neurons while simultaneously performing high-speed calcium imaging with minimal cross-talk in mice *in vivo*. Independent manipulation of two femtosecond-pulsed laser beams enabled precise control over the activated neurons with high spatiotemporal resolution recording of stimulated and nearby neurons. We performed user-selected targeting of neurons for activation with a programmable spatial light modulator[18] (SLM), allowing us to photostimulate neurons on the basis of their individual functional identities, not just genetic class. In combination with chronic window preparations[19], our approach enables high-throughput probing of the same neural circuits in awake, behaving animals over long timescales.

[1]Wolfson Institute for Biomedical Research, University College London, London, UK. [2]Department of Neuroscience, Physiology and Pharmacology, University College London, London, UK. Correspondence should be addressed to M.H. (m.hausser@ucl.ac.uk).

RECEIVED 3 AUGUST; ACCEPTED 24 NOVEMBER; PUBLISHED ONLINE 22 DECEMBER 2014; CORRECTED AFTER PRINT 6 FEBRUARY 2015; DOI:10.1038/NMETH.3217

RESULTS

Combining calcium imaging and single-cell photostimulation *in vivo*

Our design goal was to be able to selectively activate groups of individually targeted neurons based on their functional identity and then observe the response to stimulation in these neurons and the local network in an awake, behaving animal (**Fig. 1a**). We incorporated an SLM into a two-photon *in vivo* dual-beampath resonant scanning microscope in order to provide simultaneous two-photon imaging and patterned optogenetic stimulation (**Fig. 1b**). We visualized neurons co-infected with GCaMP6s, an 'ultrasensitive' green-fluorescent genetically encoded calcium indicator[20], and C1V1-2A-mCherry, a red-shifted opsin[21] (**Fig. 1c**). We recorded high-speed (30 Hz) calcium imaging movies over a field of view of 200 × 200 µm using a resonant scanning system at 920 nm and photostimulated neurons via two-photon excitation at 1,064 nm (**Fig. 1d**). We calibrated our all-optical approach by performing simultaneous cell-attached patch-clamp recordings in layer 2/3 of the mouse somatosensory cortex (n = 3 experiments). We programmed the SLM to generate a single photostimulation spot, which was scanned in a spiral fashion[22] over the neuronal cell body for 20 ms (see Online Methods). Single action potentials were reliably generated in the recorded neuron on every trial, resulting in large calcium transients in the photostimulated neuron, but not in neighboring neurons also expressing GCaMP6s and C1V1 (**Fig. 1e**). The spatial resolution of spiral photostimulation using 6 mm galvanometers (see Online Methods) was 12 µm laterally and ~24 µm axially, measured by incrementally shifting the photostimulation target (**Supplementary Fig. 1**). Action potential detection sensitivity was maintained even when we imaged the entire 200 × 200 µm field of view, and imaging at this resolution did not result in photostimulation (**Supplementary Fig. 2**). In summary, we demonstrated that our approach is capable of simultaneous sensitive calcium imaging and precise two-photon optogenetic photostimulation in the same neurons *in vivo*.

We tested an alternative method for generating single action potentials *in vivo* in cortical neurons expressing C1V1-2A-YFP via viral infection (**Supplementary Fig. 3a**). This method is possible with all commercially available two-photon microscopes. We chose a spatiotemporal photostimulation pattern of a 10 × 10 grid of sites extending slightly beyond the borders of the neuron to ensure robust action potential generation in the recorded neuron. The photostimulation laser was directed to the target sites sequentially in raster fashion (0.1 ms per site, 0.1 ms intersite interval, 20 ms total exposure time; **Supplementary Fig. 3a**), generating exactly one action potential in putative pyramidal neurons with a latency of 17.3 ± 0.7 (mean ± s.e.m.) ms, measured from photostimulation onset, as observed previously[23]. Increasing the total exposure time to 40 ms (0.2 ms per site, 0.2 ms intersite interval) generated more action potentials at longer latencies because of the increased time it took to cover the cell soma (1.4 ± 0.09 action potentials; 33.2 ± 2.1 ms latency to first action potential; n = 4 neurons, 3 animals, 57 photostimulation trials; **Supplementary Fig. 3b**). Increasing the exposure time yet further to 120 ms (1 ms per site, 0.2 ms intersite interval) generated a similar number of action potentials in the recorded neurons (1.4 ± 0.07 action potentials, 60 ± 2.6 ms latency, n = 9 neurons from four mice; 114 photostimulation trials;

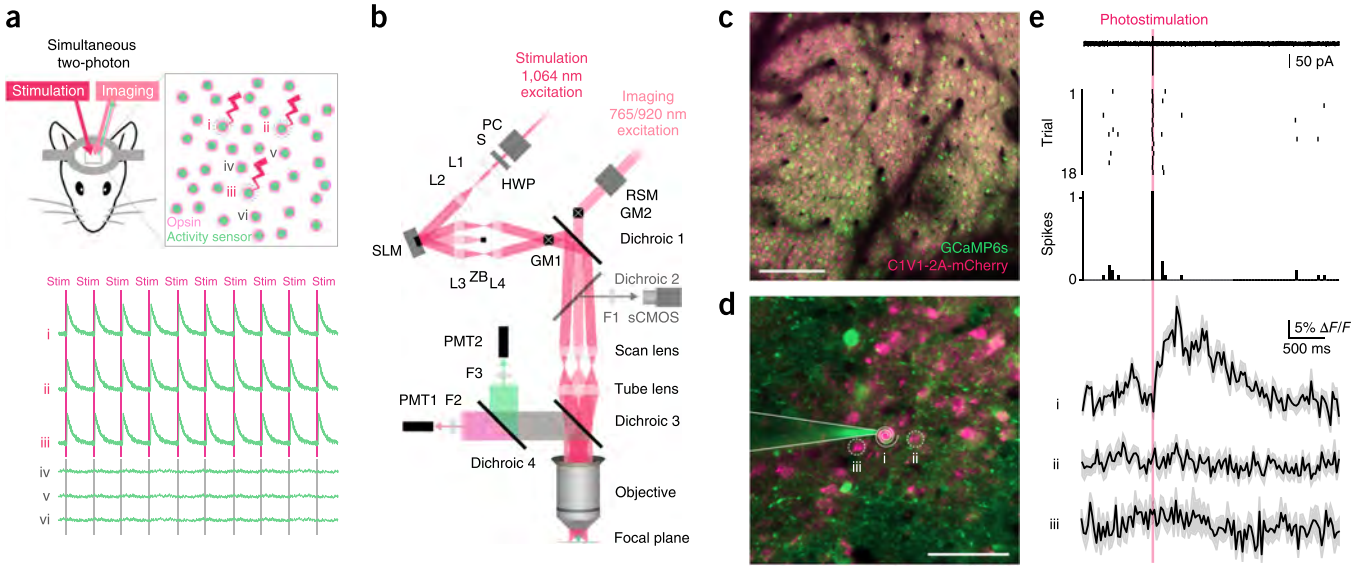

Figure 1 | Single-cell two-photon optogenetic photostimulation and single-action-potential readout *in vivo*. (**a**) Schematic illustration of the experimental goal. Top, a calcium sensor generates an optical readout of activity, and an opsin enables photostimulation. Bottom, robust and reliable photostimulation in user-selected neurons i–iii without stimulation of immediately adjacent neurons iv–vi during simultaneous recording. Stim, stimulation. (**b**) Optical layout of the SLM-based two-photon patterned photostimulation, two-photon resonant scanning, moving *in vivo* microscope. PC, Pockels cell; S, shutter; HWP, half-wave plate; L1–4, lenses; SLM, spatial light modulator; ZB, zero order block; GM1, GM2, galvanometers; RSM, resonant scanning module; F1–3: filters; PMT1, PMT2, photomultiplier tubes. (**c**) A large field of view of neurons coexpressing GCaMP6s (green) and C1V1-2A-mCherry (pink; scale bar, 100 µm). (**d**) Inset from a large field of view (200 × 200 µm) for the experiment shown in **e** (scale bar, 50 µm). A two-photon targeted cell-attached patch-clamp recording was obtained from neuron i. This neuron was targeted for optogenetic stimulation in a spiral pattern. (**e**) Top, electrophysiological recording during photostimulation trials (pink bar). Single sweep (from trial 2), raster plot, and peristimulus time histogram are shown. Bottom, calcium imaging recordings obtained simultaneously from neurons i–iii in **d** (mean ± s.e.m., n = 3 neurons).

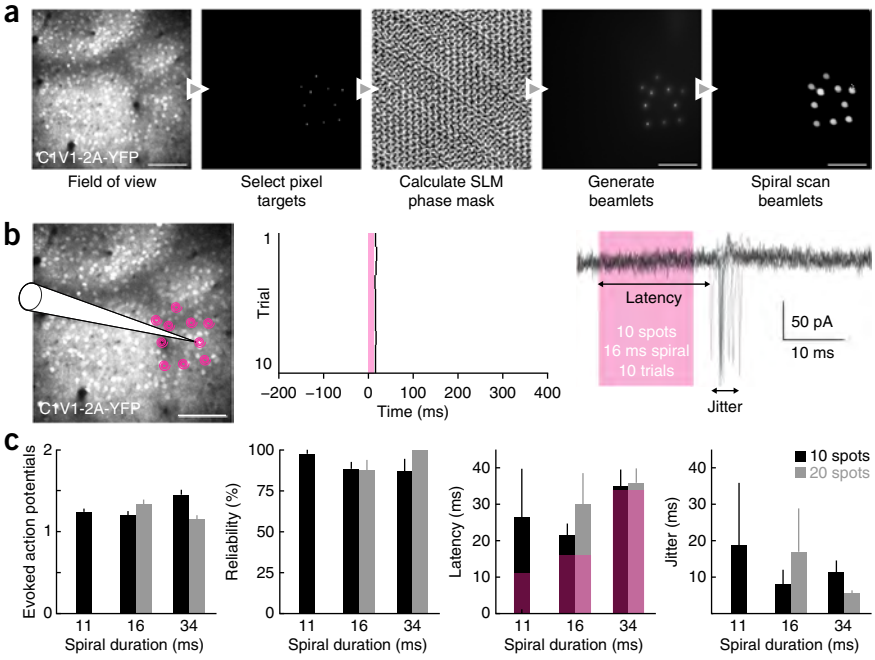

Figure 2 | Precise, concurrent photostimulation of multiple identified neurons *in vivo*. (**a**) The leftmost panel shows an example field of view of somatosensory cortex layer 2/3 neurons expressing C1V1-2A-YFP (scale bar, 100 µm). The remaining panels, from left to right, present a protocol for targeting spiral photostimulation patterns to multiple locations using the SLM and galvanometer mirrors (scale bars, 100 µm). (**b**) Left, magnification of **a** showing cell-attached patch-clamp recording configuration in which multiple locations were photostimulated while action potential generation was electrophysiologically recorded in one of the targets. Middle, raster of spike times around stimulus delivery over ten trials (photostimulation, pink bar). Right, overlaid raw data showing low latency and jitter. (**c**) Metrics evaluating performance for 10 and 20 spot photostimulation patterns and spiral photostimulations lasting 11, 16 or 34 ms. Error bars are s.e.m.; $n = 6$ neurons, 4 mice.

Supplementary Fig. 3b). Additional illumination did not result in more action potentials (perhaps as a result of opsin desensitization exhausting the restricted population of opsins available in the small photostimulation volume). For comparison, we also tested the same photostimulation paradigm on a fast-spiking putative interneuron, which responded in a similar fashion, although with a shorter latency and more action potentials, as expected from its intrinsic electrophysiological properties (3.8 ± 0.17 action potentials, 18.1 ± 1.3 ms latency, $n = 1$ neuron, 100 photostimulation trials; **Supplementary Fig. 4**).

The spatial resolution of photostimulation using the grid pattern with 3 mm galvanometers, measured by moving the pattern relative to the neuron, was 22 µm laterally and 67 µm axially (full-width at half-maximum; **Supplementary Fig. 3c**). In total, we recorded from 19 neurons in five mice while photostimulating with a range of parameters and found a reliable strategy for optically generating action potentials in individual neurons with low jitter *in vivo*.

Simultaneous photostimulation of multiple selected neurons

We used the SLM to split the photostimulation laser into individual, spatially targeted beamlets so as to activate multiple neurons concurrently[24]. Animals virally infected with C1V1-2A-YFP or C1V1-2A-mCherry showed strong expression in neurons across large territories of cortical tissue, providing many targets for simultaneous photostimulation (**Fig. 2a**). Spiral scanning of the beamlets as a group allowed more neurons to be targeted, as less power per beamlet was required (i.e., a high power density in a small beamspot was spatiotemporally multiplexed over a neuron, as opposed to an alternate strategy whereby much more power is directed on a sample, but distributed over a larger area[25]). We confirmed that our photostimulation strategy generated action potentials via simultaneous two-photon targeted cell-attached recordings when just one of the selected ten targets was positioned over a neuron (**Fig. 2b**). Spiral scans lasting 11 and 16 ms reliably generated one action potential at similar latencies (1.2 ± 0.04

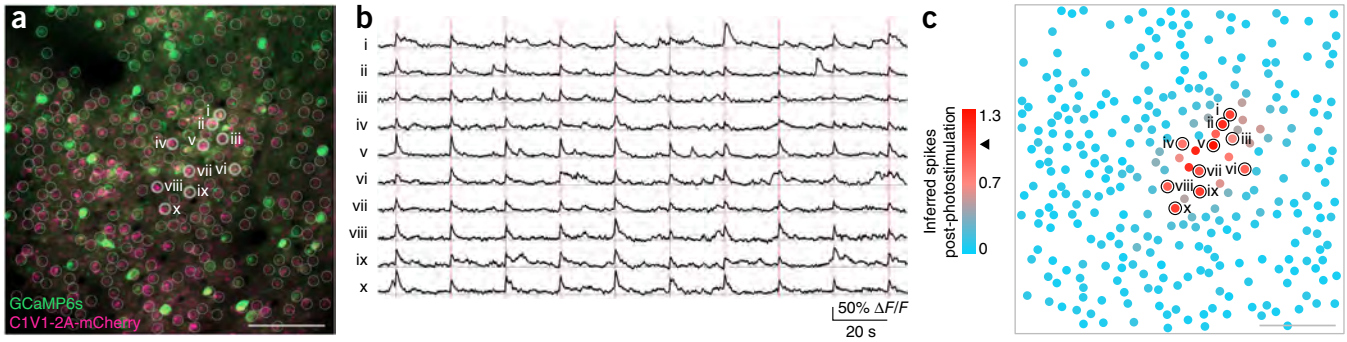

Figure 3 | Simultaneous fast calcium imaging and concurrent photostimulation of multiple neurons *in vivo*. (**a**) A field of view of neurons in layer 2/3 of somatosensory cortex colabeled with C1V1-2A-mCherry and GCaMP6s (scale bar, 100 µm). Ten neurons were targeted for simultaneous photostimulation (white circles). (**b**) Calcium transients from the ten photostimulated neurons showing the responses on all individual trials. (**c**) Color-coded plot of the strength of photostimulation in the field from panel **a** as measured by the sum of inferred spikes immediately post-stimulation. Stimulated neurons are circled in black. 300 total neurons, 120 trials, mean inferred action potentials post-photostimulation = 1.0 ± 0.1 (mean ± s.d.; black arrowhead in legend).

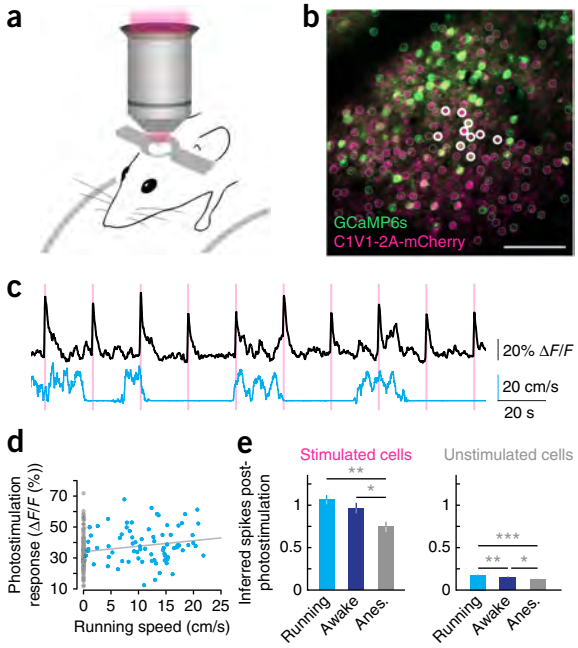

Figure 4 | Dependence of network perturbations on behavioral state. (**a**) Mice were head-fixed and allowed to run freely on a fixed-axis Styrofoam treadmill. (**b**) A field of view in which ten neurons in layer 2/3 of mouse somatosensory cortex (marked in white) were chosen for photostimulation. These and the surrounding neurons across the field of view were simultaneously observed with high-speed calcium imaging. (**c**) Top, mean calcium transient of all stimulated neurons in response to simultaneous photostimulation of ten neurons. Bottom, running speed. (**d**) Correlation between mean perturbation of responses to photostimulation and running speed. (Regression line in gray.) (**e**) Comparison of inferred spike responses to photostimulation (mean ± s.d.) during different behavioral states (n = 3 mice, 576 imaged neurons; Tukey's test for multiple comparisons; *, ** and *** denote $P < 0.05$, 0.01 and 0.001, respectively; exact P values in the text). Anes., anesthetized.

and 1.2 ± 0.05 action potentials, one or more action potentials on 98% ± 3% and 88% ± 4% of trials, 26.4 ± 13.3 and 21.4 ± 3.3 ms latency, 18.8 ± 17.1 and 8.0 ± 4.0 ms jitter (defined as the standard deviation of the latency), respectively; 107 photostimulation trials in six neurons in four animals; **Fig. 2c**). Increasing the spiral duration increased the number of action potentials generated and their latency (34 ms spiral: 1.5 ± 0.06 action potentials, one or more action potentials on 87% ± 8% of trials, 34.9 ± 4.6 ms latency, 11.3 ± 3.3 ms jitter, 93 photostimulation trials in six neurons in four animals), presumably because of the increased photostimulation exposure time and the longer time it took to cover the cell body, respectively. Increasing the number of photostimulated neurons from 10 to 20 reduced the laser power per spot, resulting in a slight increase in latency (1.3 ± 0.06 and 1.2 ± 0.05 action potentials, one or more action potentials on 88% ± 6% and 100% ± 0% of trials, 30.1 ± 8.5 and 35.9 ± 4.0 ms latency, 17.0 ± 11.9 and 5.6 ± 0.8 ms jitter for 16 ms and 34 ms spirals, respectively; 70 photostimulation trials for six recorded neurons in three animals). In summary, we demonstrated optically generated action potentials with low jitter (results comparable to those from previous *in vitro* work[23,24,26]) in 10–20 selected neurons, confirmed by recording from 11 neurons in seven animals. These experiments show that our approach can generate precisely timed action potentials in multiple, individually selected neurons using programmed patterns of photostimulation.

Network readout during targeted multineuron stimulation

We combined the all-optical approach (**Fig. 1**) with the photostimulation of multiple specified neurons (**Fig. 2**) to investigate how precisely controlled photostimulation inputs are integrated by neural populations *in vivo*. We programmed the SLM to generate ten beamlets targeted to a cluster of ten neurons. While simultaneously imaging these and the surrounding 290 neurons at 30 Hz, we photostimulated the 10 selected neurons (n = 3 mice, **Fig. 3a**). Individual target neurons showed strong and reliable responses to photostimulation (**Fig. 3b**,**c**). We performed this experiment in three mice. Only a small proportion of neighboring neurons responded (**Supplementary Fig. 5**), as expected from our and others' previous work[27,28]. Some neurons expressed GCaMP6s very strongly, as observed previously[20,29], and showed reduced responses to photostimulation (**Supplementary Fig. 6a**), although these neurons could be excluded from subsequent analysis. The response to photostimulation correlated slightly but not significantly with the expression of C1V1 (**Supplementary Fig. 6b**). In summary, we were able to optically invoke spatiotemporally precise action potentials in defined sets of neurons while simultaneously recording the responses of those neurons and many others in the same field of view.

Long-term reliability and stability of all-optical interrogation

We assessed the reliability and stability of multiple cell stimulation and readout. First, we photostimulated ten neurons (**Supplementary Fig. 7a**); then we found the same ten neurons 1 week later and photostimulated them again (**Supplementary Fig. 7b**; in three fields of view in three animals). We observed the same response to photostimulation on both days (**Supplementary Fig. 7c**). All neurons in all animals showed a highly significant coefficient of determination between their responses on day 1 and day 8 ($P = 8.5 \times 10^{-19}$; $R^2 = 0.7$ when the fit was constrained to the unity line; **Supplementary Fig. 7d**).

All-optical interrogation in different behavioral states

To demonstrate the power of our strategy for probing the functional properties of neural circuits *in vivo*, we assessed how behavioral states modulate the responsiveness of neural circuits. Locomotion is a salient modulator of neuronal activity in cortical circuits[30–32]; we therefore applied our approach to compare the local network response to photostimulation while mice were running, awake but stationary or under light isoflurane anesthesia. In our experiments we allowed awake and head-fixed mice to run freely on a fixed-axis cylinder (**Fig. 4a**) while we repeatedly photostimulated ten target neurons (**Fig. 4b**) and simultaneously recorded the response to photostimulation and running speed (**Fig. 4c**). We found a significant correlation between mean amplitude of response to photostimulation and running speed (Spearman $\rho = 0.27$, $P = 7.1 \times 10^{-5}$; n = 22 experiments; 220 total stimulations in three mice; **Fig. 4d**). We performed the same patterned stimulation in the same field of view in the same mice while the animals were awake but not running or were lightly anesthetized (**Fig. 4e**). We found a significant reduction in target neuron responses to photostimulation when animals

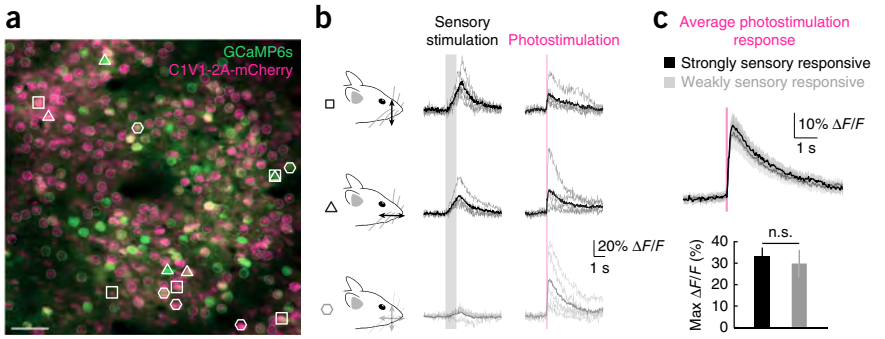

Figure 5 | Targeting neurons for optogenetic manipulation based on their individual functional signatures *in vivo*. (**a**) A field of view (scale bar, 50 µm) showing neurons coexpressing GCaMP6s (green) and C1V1-2A-mCherry (pink) in the C2 barrel of mouse somatosensory cortex. (For definitions of symbols, see **b**.) (**b**) Groups of individually identified neurons were selected for photostimulation based on their response to dorsal-ventral and rostro-caudal whisker stimulation. Five neurons that responded differently or not at all to sensory stimulation (gray shading) were simultaneously photostimulated (pink line). (**c**) Simultaneous photostimulation of five neurons responding strongly to a given sensory stimulation or weakly to both stimuli revealed similar responses (mean ± s.e.m.) to photostimulation (n = 25 strongly responsive neurons and 15 weakly responsive neurons, stimulated in groups of 5 in two fields of view in one mouse).

were anesthetized (P = 0.00099, one-way analysis of variance (ANOVA); P = 0.00082, running versus anesthetized; P = 0.029, awake versus anesthetized; Tukey's test for multiple comparisons). We observed a significant difference between all behavioral states for the responses of non-stimulated local network neurons ($P = 4.2 \times 10^{-8}$, one-way ANOVA; P = 0.0078, running versus awake; $P = 1.5 \times 10^{-8}$, running versus anesthetized; P = 0.012, awake versus anesthetized; Tukey's test for multiple comparisons; n = 3 mice, 576 imaged neurons, 30 stimulated neurons, 280 trials distributed between behavioral states; minimum 20 trials per state per mouse). These results demonstrate the robustness of our approach for perturbing neuronal networks during ongoing activity and different behavioral states.

Optogenetic manipulation targeted to functional ensembles

Our approach allowed us to target different groups of neurons within the population on the basis of their individual functional properties. To achieve this goal, first we performed intrinsic imaging to identify barrel C2 in the somatosensory cortex (**Fig. 5a**). Next, two-photon imaging of the responses of individual neurons to sensory stimulation within the barrel revealed neurons that responded strongly or weakly to particular stimulation orientations (**Fig. 5b**). We targeted photostimulation to five neurons within each of the three groups while the animal was awake and running on a Styrofoam treadmill. The response to photostimulation was not significantly different between the strongly sensory-responsive (both groups) and weakly sensory-responsive groups (maximum $\Delta F/F$ response to photostimulation: 33% ± 4% and 30% ± 6%, p = 0.55, Mann-Whitney test; n = 25 and 15 strongly and weakly sensory-responsive neurons, respectively, in two fields of view; **Fig. 5c**). This experiment highlights the utility of our approach for activating functionally defined ensembles of neurons in the awake, behaving animal.

DISCUSSION

Probing neural circuits at the spatial and temporal resolution at which they function is crucial to understanding how populations of neurons work together to drive behavior. Optical approaches allow this to be achieved in a minimally invasive manner. We have developed an all-optical strategy for activating and recording the same neurons with cellular resolution in mice *in vivo* by combining two-photon optogenetics and calcium imaging. The combination of indicator sensitivity and lack of spectral overlap between the optogenetic excitation and GCaMP6s emission wavelengths minimizes the stimulation artifact and enables single-spike precision. The optical nature of the approach, combined with a chronic window preparation, provides both the flexibility of being able to select individual neurons for stimulation while the animal is awake and behaving under the microscope over weeks to months and the ability to target the activation of multiple neurons that are activated during a behavioral task. Our method thus enables high-throughput, flexible and long-term optical interrogation of neural circuits in the mammalian brain *in vivo*. The ability to target neurons based on their functional signature will enable one to replay and manipulate natural patterns of activity in neural circuits[1]. This strategy provides a significant advance over previous approaches in which neurons were defined either anatomically or genetically, as it allows one to target individual neurons on the basis of their specific functional properties. The ability to simultaneously manipulate and read out activity from functionally defined neuronal ensembles will open up new avenues for optogenetic experiments.

Previous methods for single-neuron-precision optogenetic manipulation relied on raster or spiral scanning methods to spatiotemporally multiplex a small excitation beamspot over a cell body[22–24,33] or illumination of the entire cell body at once via holography and/or temporal focusing to provide optical sectioning[3,26,34,35]. All of these approaches have thus far been demonstrated only *in vitro*, aside from our previous proof-of-principle experiments[23] showing that the two-photon optogenetic excitation strategy could work *in vivo* and recent work that was published while this work was in review[3]. Other work has shown that temporal focusing combined with general phase contrast enables action potential generation via two-photon excitation of channelrhodopsin deep in brain slices[36].

Our approach, combining SLM-based beam splitting with spiral scanning, allows one to simultaneously address a large population of neurons *in vivo*. There is a tradeoff between the number of neurons that can be simultaneously addressed and how quickly a simultaneous stimulation pattern can be performed, dictated by the power and time required for a given spatiotemporal multiplexing strategy. In alternative holographic and/or temporal focusing–based approaches, simultaneous photostimulations can be achieved more quickly, at the cost of addressing fewer neurons per 'shot'. The advantage of such alternative strategies may be more efficient shaping of the temporal profile of the response pattern. Our strategy attempts to maximize the number of neurons per stimulation while minimizing the photostimulation time by splitting

the beam and using a fast scanning strategy to photostimulate neurons. Thus, while all of these technologies are currently under active development, our approach is well suited for the generation of synchronous activity among ensembles of neurons, which can be performed at high rates in a sequence with this method. We expect that the underlying biological question being addressed will dictate the choice among these different approaches *in vivo*.

Our all-optical, dual two-photon approach combining fast readout with high-speed calcium imaging of the most recent 'ultrasensitive' calcium indicator[20] drastically reduces the cross-talk problem observed in previous all-optical approaches relying on one-photon excitation[5–7]. These approaches require blocking of the readout during photostimulation, resulting in the loss of crucial data. Additionally, the ability to directly observe neuronal locations and target neurons with single-cell precision removes any confusion about which cells are directly stimulated and which are downstream[14,15], which has been a problem with other simultaneous readout and manipulation strategies relying on the combination of electrophysiology and optogenetics, such as the use of optrodes[11–13]. Further development of new molecular tools[37], including characterization of their two-photon excitation, will enable their integration into the *in vivo* approach presented here. In addition, advances in faster and more complex imaging methods[38–40] and analysis[41] could be incorporated into the readout side of the approach.

Our ability to read out and manipulate activity in the same population of neurons provides us with the unprecedented opportunity to target optogenetic manipulation on the basis of the functional signature of the neurons. Previously, optogenetic manipulations could be targeted based on genetic and/or anatomical identity alone[42], or on *c-fos* expression[43], which provides only a very indirect readout of activity and lacks temporal precision. Here we describe proof-of-principle experiments showing that we were able to use a detailed functional characterization of the response of neurons to different sensory stimuli to enable targeting of specific ensembles in the population. This will allow optogenetic manipulation to be targeted with far greater precision than previously possible, enabling investigation of the neural code in only those neurons within a population exhibiting a specific functional signature during sensory processing or defined behaviors. Future work using this approach should provide fundamental new insights into information processing in neural circuits *in vivo*.

METHODS

Methods and any associated references are available in the online version of the paper.

Note: Any Supplementary Information and Source Data files are available in the online version of the paper.

ACKNOWLEDGMENTS

We thank M. Pachitariu, C. Stringer, S. Turaga, M. London and N. Pettit for helpful discussion, analysis routines and software; C. Wilms, C. Schmidt-Hieber, A. Roth, B. Clark, I. Bianco, S. Smith, B. Judkewitz and D. Peterka for discussion and comments on the manuscript; the staff at Bruker Corporation (formerly Prairie Technologies) for enabling customization of the microscope; M. Lochrie at the Stanford Neuroscience Gene Vector and Virus Core (grant no. P30 NS069375-01A1) for advice on use of AAVdj; and K. Deisseroth (Stanford University) for plasmids and access to AAVdj virus. This work was supported by grants from the Wellcome Trust, the Gatsby Charitable Foundation, the European Commission (Marie Curie International Incoming Fellowship grant no. 328048), the European Molecular Biology Organization, the Medical Research Council and the European Research Council.

AUTHOR CONTRIBUTIONS

A.M.P., L.E.R. and H.W.P.D. performed experiments and analyzed data.
A.M.P., L.E.R., H.W.P.D. and M.H. designed the study and wrote the paper.

COMPETING FINANCIAL INTERESTS

The authors declare no competing financial interests.

1. Packer, A.M., Roska, B. & Hausser, M. Targeting neurons and photons for optogenetics. *Nat. Neurosci.* **16**, 805–815 (2013).
2. Grienberger, C. & Konnerth, A. Imaging calcium in neurons. *Neuron* **73**, 862–885 (2012).
3. Rickgauer, J.P., Deisseroth, K. & Tank, D.W. Simultaneous cellular-resolution optical perturbation and imaging of place cell firing fields. *Nat. Neurosci.* **17**, 1816–1824 (2014).
4. Huber, D. *et al.* Sparse optical microstimulation in barrel cortex drives learned behaviour in freely moving mice. *Nature* **451**, 61–64 (2008).
5. Fajardo, O., Zhu, P. & Friedrich, R.W. Control of a specific motor program by a small brain area in zebrafish. *Front. Neural Circuits* **7**, 67 (2013).
6. Wilson, N.R., Runyan, C.A., Wang, F.L. & Sur, M. Division and subtraction by distinct cortical inhibitory networks *in vivo*. *Nature* **488**, 343–348 (2012).
7. Zhang, Y.P. & Oertner, T.G. Optical induction of synaptic plasticity using a light-sensitive channel. *Nat. Methods* **4**, 139–141 (2007).
8. Akerboom, J. *et al.* Genetically encoded calcium indicators for multi-color neural activity imaging and combination with optogenetics. *Front. Mol. Neurosci.* **6**, 2 (2013).
9. Anselmi, F., Ventalon, C., Begue, A., Ogden, D. & Emiliani, V. Three-dimensional imaging and photostimulation by remote-focusing and holographic light patterning. *Proc. Natl. Acad. Sci. USA* **108**, 19504–19509 (2011).
10. Dal Maschio, M. *et al.* Simultaneous two-photon imaging and photo-stimulation with structured light illumination. *Opt. Express* **18**, 18720–18731 (2010).
11. LeChasseur, Y. *et al.* A microprobe for parallel optical and electrical recordings from single neurons *in vivo*. *Nat. Methods* **8**, 319–325 (2011).
12. Anikeeva, P. *et al.* Optetrode: a multichannel readout for optogenetic control in freely moving mice. *Nat. Neurosci.* **15**, 163–170 (2011).
13. Royer, S. *et al.* Multi-array silicon probes with integrated optical fibers: light-assisted perturbation and recording of local neural circuits in the behaving animal. *Eur. J. Neurosci.* **31**, 2279–2291 (2010).
14. Lima, S.Q., Hromadka, T., Znamenskiy, P. & Zador, A.M. PINP: a new method of tagging neuronal populations for identification during *in vivo* electrophysiological recording. *PLoS ONE* **4**, e6099 (2009).
15. Kravitz, A.V., Owen, S.F. & Kreitzer, A.C. Optogenetic identification of striatal projection neuron subtypes during *in vivo* recordings. *Brain Res.* **1511**, 21–32 (2013).
16. Svoboda, K., Denk, W., Kleinfeld, D. & Tank, D.W. *In vivo* dendritic calcium dynamics in neocortical pyramidal neurons. *Nature* **385**, 161–165 (1997).
17. Denk, W., Strickler, J.H. & Webb, W.W. Two-photon laser scanning fluorescence microscopy. *Science* **248**, 73–76 (1990).
18. Nikolenko, V. *et al.* SLM microscopy: scanless two-photon imaging and photostimulation with spatial light modulators. *Front. Neural Circuits* **2**, 5 (2008).
19. Holtmaat, A. *et al.* Long-term, high-resolution imaging in the mouse neocortex through a chronic cranial window. *Nat. Protoc.* **4**, 1128–1144 (2009).
20. Chen, T.W. *et al.* Ultrasensitive fluorescent proteins for imaging neuronal activity. *Nature* **499**, 295–300 (2013).
21. Yizhar, O. *et al.* Neocortical excitation/inhibition balance in information processing and social dysfunction. *Nature* **477**, 171–178 (2011).
22. Rickgauer, J.P. & Tank, D.W. Two-photon excitation of channelrhodopsin-2 at saturation. *Proc. Natl. Acad. Sci. USA* **106**, 15025–15030 (2009).
23. Prakash, R. *et al.* Two-photon optogenetic toolbox for fast inhibition, excitation and bistable modulation. *Nat. Methods* **9**, 1171–1179 (2012).
24. Packer, A.M. *et al.* Two-photon optogenetics of dendritic spines and neural circuits. *Nat. Methods* **9**, 1202–1205 (2012).

25. Peron, S. & Svoboda, K. From cudgel to scalpel: toward precise neural control with optogenetics. *Nat. Methods* **8**, 30–34 (2011).
26. Papagiakoumou, E. *et al.* Scanless two-photon excitation of channelrhodopsin-2. *Nat. Methods* **7**, 848–854 (2010).
27. Kwan, A.C. & Dan, Y. Dissection of cortical microcircuits by single-neuron stimulation *in vivo*. *Curr. Biol.* **22**, 1459–1467 (2012).
28. London, M., Roth, A., Beeren, L., Hausser, M. & Latham, P.E. Sensitivity to perturbations *in vivo* implies high noise and suggests rate coding in cortex. *Nature* **466**, 123–127 (2010).
29. Tian, L. *et al.* Imaging neural activity in worms, flies and mice with improved GCaMP calcium indicators. *Nat. Methods* **6**, 875–881 (2009).
30. Fu, Y. *et al.* A cortical circuit for gain control by behavioral state. *Cell* **156**, 1139–1152 (2014).
31. Niell, C.M. & Stryker, M.P. Modulation of visual responses by behavioral state in mouse visual cortex. *Neuron* **65**, 472–479 (2010).
32. Schneider, D.M., Nelson, A. & Mooney, R. A synaptic and circuit basis for corollary discharge in the auditory cortex. *Nature* **513**, 189–194 (2014).
33. Zhu, P. *et al.* Optogenetic dissection of neuronal circuits in zebrafish using viral gene transfer and the Tet system. *Front. Neural Circuits* **3**, 21 (2009).
34. Andrasfalvy, B.K., Zemelman, B.V., Tang, J. & Vaziri, A. Two-photon single-cell optogenetic control of neuronal activity by sculpted light. *Proc. Natl. Acad. Sci. USA* **107**, 11981–11986 (2010).
35. Losonczy, A., Zemelman, B.V., Vaziri, A. & Magee, J.C. Network mechanisms of theta related neuronal activity in hippocampal CA1 pyramidal neurons. *Nat. Neurosci.* **13**, 967–972 (2010).
36. Papagiakoumou, E. *et al.* Functional patterned multiphoton excitation deep inside scattering tissue. *Nat. Photonics* **7**, 274–278 (2013).
37. Hochbaum, D.R. *et al.* All-optical electrophysiology in mammalian neurons using engineered microbial rhodopsins. *Nat. Methods* **11**, 825–833 (2014).
38. Ahrens, M.B. *et al.* Brain-wide neuronal dynamics during motor adaptation in zebrafish. *Nature* **485**, 471–477 (2012).
39. Prevedel, R. *et al.* Simultaneous whole-animal 3D imaging of neuronal activity using light-field microscopy. *Nat. Methods* **11**, 727–730 (2014).
40. Quirin, S., Jackson, J., Peterka, D.S. & Yuste, R. Simultaneous imaging of neural activity in three dimensions. *Front. Neural Circuits* **8**, 29 (2014).
41. Freeman, J. *et al.* Mapping brain activity at scale with cluster computing. *Nat. Methods* **11**, 941–950 (2014).
42. Yizhar, O., Fenno, L.E., Davidson, T.J., Mogri, M. & Deisseroth, K. Optogenetics in neural systems. *Neuron* **71**, 9–34 (2011).
43. Liu, X. *et al.* Optogenetic stimulation of a hippocampal engram activates fear memory recall. *Nature* **484**, 381–385 (2012).

ONLINE METHODS

All surgical procedures were carried out under license from the UK Home Office in accordance with the Animal (Scientific Procedures) Act 1986. C57/BL6 mice (*Mus musculus*) approximately 4 weeks to 3 months old of both sexes were used without randomization. Animals were anesthetized with an intraperitoneal injection of a ketamine-xylazine mixture (0.1 and 0.01 mg g^{-1} body weight, respectively) or with isoflurane during surgical procedures.

Viral injections, headplate and chronic window installation. Craniotomies were drilled (NSK UK Ltd.) over barrel cortex (right hemisphere, 2 mm posterior from and 3.5 mm lateral of bregma, 0.5 mm in diameter). Calibrated injection pipettes beveled to a sharp point (inner diameter: ~15 µm) were coupled to a hydraulic injection apparatus driven by a syringe pump (Harvard Apparatus). Virus (AAV2-CaMKIIa-C1V1(E162T)-p2A-EYFP, AAVdj-CaMKIIa-C1V1(E162T)-TS-P2A-mCherry-WPRE[44] or AAV1-Syn-GCaMP6s-WPRE-SV40[20]) was front-loaded into the injection pipette and injected at a rate of 0.1 µl min^{-1} into layer 2/3 (~300 µm deep). Animals that received two separate injections were first injected with 1 µl of virus, and then the scalp incision was closed with Vetbond (3M). Subsequent injections, also 1 µl, were performed through the same craniotomy site, which was still visible 24 days later. Animals singly injected received 1 µl of virus. Co-injected animals were injected with a mixture containing 0.1 µl GCaMP6s virus and 0.9 µl C1V1-2A-mCherry virus.

For chronic experiments, the scalp was removed bilaterally from the midline to the temporalis muscles, and a metal headplate with a 5 mm circular imaging well was fixed to the skull overlying somatosensory cortex with dental cement (Super-Bond C&B, Sun-Medical) before virus injection. Intrinsic imaging[45] was performed to further localize the injection site to the C2 barrel in certain experiments. The C2 whisker was threaded into a trimmed glass pipette glued to a piezoeletric actuator (Physik Instrumente). The actuator was programmed to oscillate at 10 Hz for 4 s with a 20 s interstimulus interval. The brain was perfused with sterile external solution (150 mM NaCl, 2.5 mM KCl, 10 mM HEPES, 2 mM $CaCl_2$, 1 mM $MgCl_2$) to make the skull semitransparent and imaged with a CCD (charge-coupled device) camera (Pike F-032b, Allied Vision Technologies) while a red light-emitting diode (LED) illuminated the surface. An increase in reflectance from the brain indicated the barrel, which could be localized relative to the blood vessel pattern as visualized with a green LED. After virus injection (see above), a 3 mm circular craniotomy was performed during which any bleeding was washed away with sterile external solution or stanched with Sugi-sponges (Sugi, Kettenbach). Cranial windows composed of a 3 mm circular glass coverslip cemented to a 2 mm square glass coverslip (UQG Optics) with UV-curable optical cement (NOR-61, Norland Optical Adhesive) were press-fit into the craniotomy, sealed to the skull by a thin layer of cyanoacrylate (VetBond) and fixed in place by dental cement.

Following all surgical procedures, animals recovered for at least 7 days with post-operative administration of 0.7 µl ml^{-1} Rimadyl and 4 µl ml^{-1} Baytril in drinking water.

Titration of calcium indicator expression. The sensitivity of the readout in our all-optical approach depended heavily on the expression of GCaMP6s. To assess the stability of calcium indicator expression, we injected animals with GCaMP6s virus at three viral titers: 3.22×10^{13} genomes per milliliter of stock and lower titer solutions of 3.22×10^{12} and 3.22×10^{11} genomes per milliliter diluted in a buffer solution (20 mM Tris, pH 8.0, 140 mM NaCl, 0.001% pluronic F-68). 100 nl of virus was injected at 0.1 µl min^{-1} into L2/3 barrel cortex (2 mm posterior and 3.5 mm lateral of bregma, 300 µm below dura). We divided 18 adult (P60–P80) C57/BL6 mice of both sexes into three cohorts of six mice each and injected each cohort with one of the above dilutions. Each six-animal viral-titer cohort was then divided such that within each cohort, two animals could be used for each of three time points: 1 week, 2 weeks and 3 weeks post-injection. At each of these time points an acute craniotomy was performed to enable two-photon imaging (see below) under isoflurane anesthesia (5% for induction, 1.5% for surgery and 0.5% for imaging). Two-photon images tiling the infection site were taken at 10 µm intervals from the cortical surface to a maximum depth of 500 µm (depending on the extent of expression). Acute imaging was used in order to minimize potential confounding artifacts introduced by chronic window implantation. The crucial parameter was a reduction in virus titer to 10% of the original level (i.e., 10^{12} genomes per milliliter), which resulted in stable expression as long as 12 weeks post-injection (**Supplementary Fig. 8**). Next, we confirmed single-action-potential resolution by performing two-photon targeted cell-attached recordings while imaging at 60 Hz ($n = 4$ neurons; **Supplementary Fig. 9a**). We found that the number of spikes in a burst occurring within a 250 ms window could be reliably reported when we integrated the results of the deconvolution algorithm[46] (**Supplementary Fig. 9b**). Integrating the result of this inference over a 433 ms window resulted in the best performance as defined by the strength of the correlation between the true number of spikes and the inferred number of spikes (**Supplementary Fig. 9c**). We also quantified the hit rate (94% ± 3%) and false positive rate (7% ± 6%) on three neurons as in ref. 20, not including one held-out neuron on which we based the classifier (**Supplementary Fig. 9d**).

The need to reduce the titer of the GCaMP6s-producing virus meant we could dilute it directly with the virus expressing C1V1-2A-mCherry (see above). After this mixture of viruses had been injected into the animals during a single surgical procedure, a chronic window was installed to provide long-term optical access to the cortical tissue of interest. After 5 weeks, we observed co-labeling of neurons with both GCaMP6s and C1V1-2A-mCherry, which were easily spectrally separated based on emission wavelength.

Cell-attached targeted patch-clamp recordings. Headplate installation was performed as described above. Two-photon targeted patch-clamp recordings[47,48] were obtained using glass pipettes pulled from borosilicate glass (~5 M pipette resistance) and filled with external solution. Signals were amplified on a MultiClamp 700a (Molecular Devices), filtered with a Bessel filter above 4 kHz and recorded at 20 kHz with custom software (PackIO[49]) written in LabView (National Instruments).

Imaging and photostimulation. Two-photon imaging was performed by raster scanning a femtosecond-pulsed laser beam (Chameleon Ultra II, Coherent) via standard or resonant

galvanometer raster scanning with a moving *in vivo* microscope (Bruker Corporation, formerly Prairie Technologies). A 16×/0.8-NA objective (Nikon) was used for all experiments. GCaMP6s was imaged with an excitation wavelength of 920 nm during calcium imaging, and mCherry was imaged at 765 nm.

A reflective spatial light modulator (SLM) (7.68 × 7.68 mm active area, 512 × 512 pixels, optimized for 1,064 nm, Meadowlark Optics/Boulder Nonlinear Systems) was coupled to the microscope using a lightpath similar to that for an *in vitro* microscope[18], but with the significant difference that the entire microscope, including SLM and beam expansion telescope, moves relative to the sample. The power was controlled by a Pockels cell (PC (acronyms refer to **Fig. 1b**)) (Conoptics Ltd.) and shutter (S) (Vincent Associates), resized using a beam-expanding telescope (L1 (f = 50 mm) and L2 (f = 200 mm), plano-convex lenses, Thorlabs) to fill the SLM active area and polarization maximized for diffraction efficiency from the SLM with a half-wave plate (HWP) (WPH10M-1064, Thorlabs). The SLM was relayed to the photostimulation galvanometers (GM1, galvanometer mirror pair, 3 or 6 mm, Cambridge Technology, integrated into dual beam Ultimate microscope by Bruker Corp. (formerly Prairie Technologies)) via a telescope (L3, 1 inch achromatic doublet, f = 400 or 250 mm; L4, 2 inch achromatic doublet, f = 150 mm) with a zero order block (ZB) (coverslip with foil) positioned at the location of the focus of the first lens. The imaging path was scanned with a second pair of galvanometer mirrors (GM2, 6 mm, Cambridge Technology, integrated by Bruker Corp.) and could also be scanned along the fast axis by a resonant scanning galvanometer mirror (RSM) (Cambridge Technology, integrated by Bruker Corp.) relayed onto GM2. The beam-combining dichroic is a 1,030 nm short-pass (Dichroic 1, T1030SP, Chroma Technology). An optional dichroic (Dichroic 2, 660 nm long-pass, 660LP, Chroma) can be used to image the SLM beamlets in widefield mode on the scientific complementary metal-oxide semiconductor (sCMOS) camera only when Dichroic 3 (700 nm long-pass, T700lpxxr-xxt, Chroma) is removed. The additional filters, lenses and detectors are as follows: F1 = 675/67 nm bandpass filter (Semrock); sCMOS camera = ORCA-Flash4.0 (Hamamatsu); Scan lens = focal length 75 mm; Tube lens = focal length 180 mm; Dichroic 4 = 575LP (HQ575dcxr, Chroma); F2 = 525/70 nm bandpass filter (525/70m-2P, Chroma); F3 = 607/45 nm bandpass filter (607/45m-2P, Chroma); PMT1 = multi-alkali photomultiplier tube (Hamamatsu); PMT2 = GaAsP photomultiplier tube (Hamamatsu); Objective = 16×/0.8-NA (Nikon).

A computer running BNS_DVI Version 1.3 (Meadowlark Optics/Boulder Nonlinear Systems) displayed the phase mask on the SLM via an NVIDIA GeForce GTX 660 Ti graphics card and digital visual interface cable connected to the SLM driver electronics (Meadowlark Optics/Boulder Nonlinear Systems). The manufacturer-supplied lookup table converted pixel values to voltages driving the liquid crystal active area of the SLM. The zero order beam was blocked at the focus of L3 with a small piece of foil glued to a coverslip (**Fig. 1b**).

The excitation source for the photostimulation path was a femtosecond-pulsed laser fixed at 1,064 nm (total output, 5 watts; pulse width, 250–400 fs; Fianium Ltd.) or 1,055 nm (total output, 2.3 watts; pulse width, 100 fs; Coherent). The Gerchberg-Saxton (GS) algorithm[50] was used to calculate phase masks to be displayed on the SLM that would result in the desired pattern with individual beams on each targeted neuron. We found that the diffraction efficiency to targets situated at the periphery of the field of view, which required the generation of large angles by the SLM, was lower than for targets at the center of the field of view with the standard GS algorithm. This effect was likely due to the increasing impact of interpixel cross-talk in our SLM, as diffracting to large angles requires higher resolution phase masks (smaller diffracting features) that increase chromatic aberration and are more prone to interpixel cross-talk because of the greater variation in neighboring pixel values. A linear weighting of desired spot intensity prior to the GS algorithm was sufficient to counteract this effect and resulted in sufficiently homogeneous power distribution (<6% s.d.) among targets. The positioning of these beams relative to the two-photon images of the neurons was registered using a widefield sCMOS (scientific complementary metal-oxide semiconductor) camera (ORCA-Flash4.0, Hamamatsu), which imaged the sample plane via the objective and tube lens, while a homogeneously fluorescent sample was photostimulated. Alternatively, the photostimulation beams could be registered by burning a homogeneously fluorescent sample that could be visualized by the two-photon imaging laser. Spiral photostimulation patterns (three rotations, 20 µm diameter) were generated by moving all beamlets simultaneously with a pair of galvanometer mirrors conjugate to the SLM plane. Power on sample for photostimulation using a grid pattern ranged from 28 to 150 mW, but was generally 100 mW (for all experiments in **Supplementary Fig. 3**). Power on sample for spiral photostimulation experiments ranged from 20 to 80 mW. The power distribution was even across beamlets generated by the SLM (59 ± 3 mW, n = 3 patterns) as measured on sample by loading phase masks and blocking all but a single beamlet near the focus of L3 (see **Fig. 1b**).

In longitudinal experiments, the same field of view could be found over weeks based on the blood vessel pattern observed under the chronic window. The chronic window allowed visualization of a 2 × 2 mm area of cortex, and the maximum field of view allowed by two-photon imaging was 832 × 832 µm. Thus, it was straightforward to localize the same general area based on large blood vessels visualized through the eyepieces of the microscope. Afterward, images at high resolution obtained via two-photon imaging could be precisely matched to images from previous sessions based on blood vessels and any uniquely shaped processes or strongly labeled neurons. Micrometer-scale resolution was confirmed by comparing two high-resolution images such as in **Figure 4a**,**b**.

Sensory stimulation and behavior. Animals were gradually acclimatized to head-fixation if necessary and trained to sit passively in the apparatus. Animals generally ran freely on the Styrofoam treadmill while the running speed was measured with a rotary encoder on the axle. Whisker stimulation, which occurred under isoflurane anesthesia, consisted of either one-second-long 10 Hz stimulation with a one-dimensional piezoelectric actuator (Physik Instrumente) or one-second-long, random, white-noise filtered stimuli with a two-dimensional piezoelectric actuator (Noliac) onto which a capillary tube was glued as a guide for an individual whisker.

Analysis. Movement correction was performed on all calcium imaging movies using a discrete Fourier transform (DFT)–based

doi:10.1038/nmeth.3217

algorithm[51]. This algorithm computes the cross-correlation between two images via selective upsampling with a matrix-multiply DFT, thus increasing speed and reducing memory requirements. Contours defining neuronal somata were selected by hand using both GCaMP and C1V1 channels. Spike inference was performed with a fast non-negative deconvolution algorithm, for which the only required parameter was the imaging time step[46]. Analyses were performed with MATLAB and ImageJ; statistical tests were performed with Prism or MATLAB. All values are mean ± s.e.m. unless otherwise noted.

44. Grimm, D. *et al. In vitro* and *in vivo* gene therapy vector evolution via multispecies interbreeding and retargeting of adeno-associated viruses. *J. Virol.* **82**, 5887–5911 (2008).
45. Grinvald, A., Lieke, E., Frostig, R.D., Gilbert, C.D. & Wiesel, T.N. Functional architecture of cortex revealed by optical imaging of intrinsic signals. *Nature* **324**, 361–364 (1986).
46. Vogelstein, J.T. *et al.* Fast nonnegative deconvolution for spike train inference from population calcium imaging. *J. Neurophysiol.* **104**, 3691–3704 (2010).
47. Kitamura, K., Judkewitz, B., Kano, M., Denk, W. & Hausser, M. Targeted patch-clamp recordings and single-cell electroporation of unlabeled neurons *in vivo*. *Nat. Methods* **5**, 61–67 (2008).
48. Komai, S., Denk, W., Osten, P., Brecht, M. & Margrie, T.W. Two-photon targeted patching (TPTP) *in vivo*. *Nat. Protoc.* **1**, 647–652 (2006).
49. Packer, A.M. *Understanding the nervous system as an information processing machine: dense, nonspecific, canonical microcircuit architecture of inhibition in neocortex and a neural circuit for angular velocity computation*. PhD thesis, Columbia University (2011).
50. Gerchberg, R.W. & Saxton, W.O. A practical algorithm for the determination of the phase from image and diffraction plane pictures. *Optik* (*Stuttg.*) **35**, 237–250 (1972).
51. Guizar-Sicairos, M., Thurman, S.T. & Fienup, J.R. Efficient subpixel image registration algorithms. *Opt. Lett.* **33**, 156–158 (2008).

Corrigendum: Simultaneous all-optical manipulation and recording of neural circuit activity with cellular resolution *in vivo*

Adam M Packer, Lloyd E Russell, Henry W P Dalgleish & Michael Häusser
***Nat. Methods* 12, 140–146 (2015); published online 22 December 2014; corrected after print 6 February 2015**

In the version of this article initially published, the size of the scale bar reported in the legend of Figure 3a was incorrect. The correct size is 100 µm, not 50 µm. In addition, the volume of injected virus in the Online Methods section "Titration of calcium indicator expression" had the incorrect unit. The correct volume is 100 nl, not 100 µl. The errors have been corrected in the HTML and PDF versions of the article.

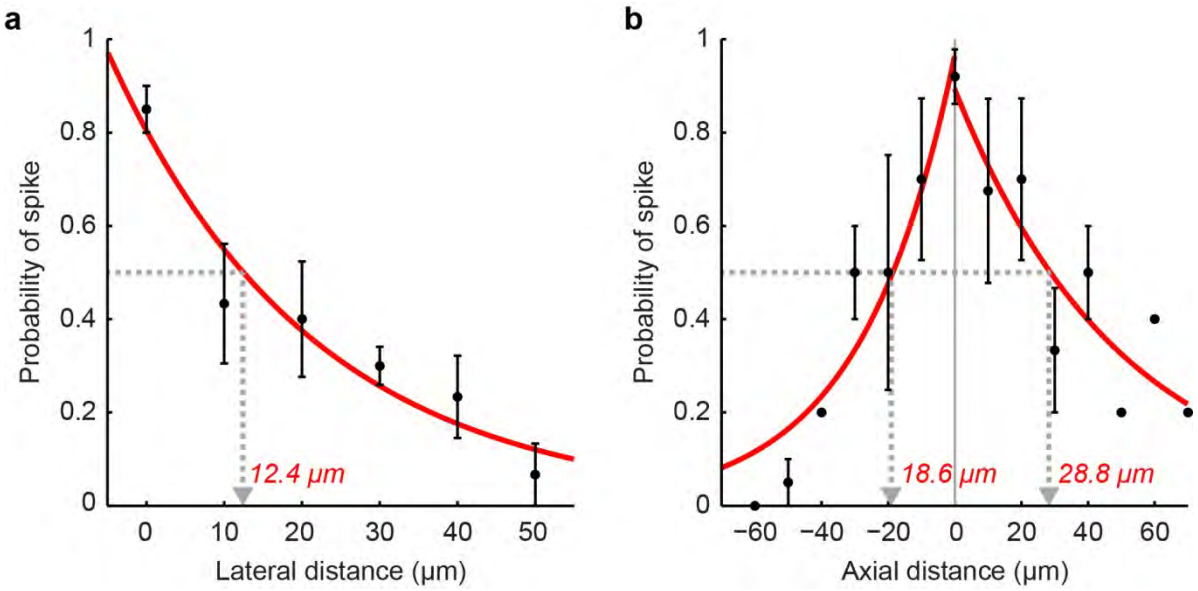

Supplementary Figure 1

Spatial resolution of spiral two-photon photostimulation *in vivo*

(a) Lateral resolution of action potential photostimulation of a layer 2/3 barrel cortex neuron in vivo using a single spot generated by the SLM scanned in the 20 µm spiral pattern (using 6 mm galvos; see Methods, n = 6 neurons).

(b) Same as above for axial resolution (n = 5 neurons). The asymmetry results from the fact that as the photostimulation pattern is directed deeper than the neuron (negative values), the probability of action potential generation drops more sharply.

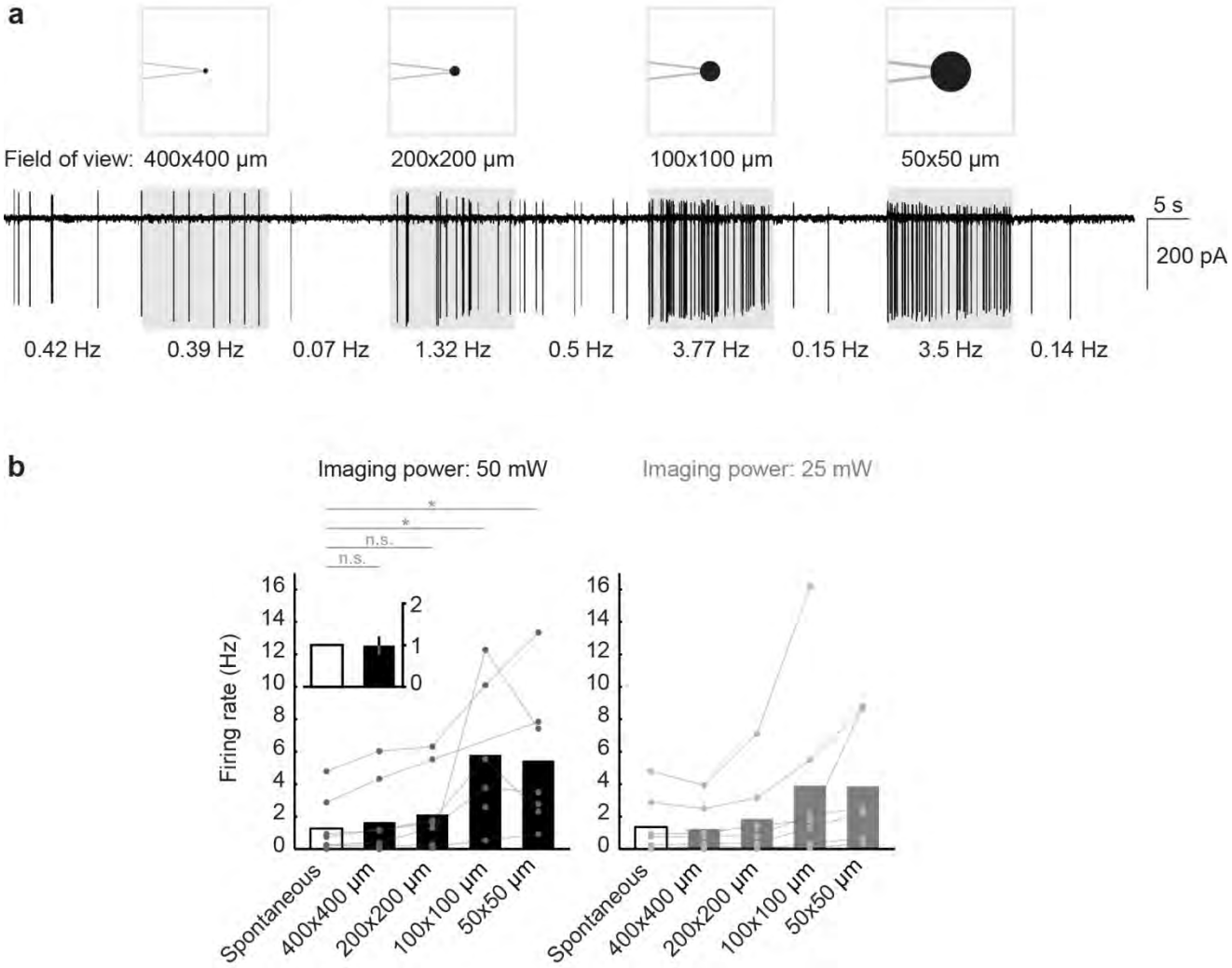

Supplementary Figure 2

Imaging over large fields of view does not cause photostimulation

(a) Example cell-attached patch clamp recording from one neuron. Periods of imaging are indicated by the shaded regions. Imaging conditions are indicated above the trace (schematic field of view shows a pipette and the recorded cell). Imaging was performed at 30 Hz with 920 nm excitation (see Methods) but the size of the field of view (optical zoom) was changed.

(b). There is no significant difference between spontaneous firing rate and that while imaging a 400x400 µm field of view at 50 mW power on sample (the conditions used in this paper; Friedman test, post hoc Dunn's multiple comparison test). Inset shows firing rates while imaging a 400x400 µm field of view, normalized to the recorded cells spontaneous firing rate; error bars represent SEM. Although the 920 nm light used for imaging is less than one-third as effective as the 1064 nm wavelength at stimulating the C1V1 opsin (Prakash et al 2012), sufficient current does accumulate in the neuron and surrounding local network when imaging at higher optical zooms. This type of stimulation could be used to optogenetically generate activity in localized circuits. n = 8 recorded neurons, 3 mice.

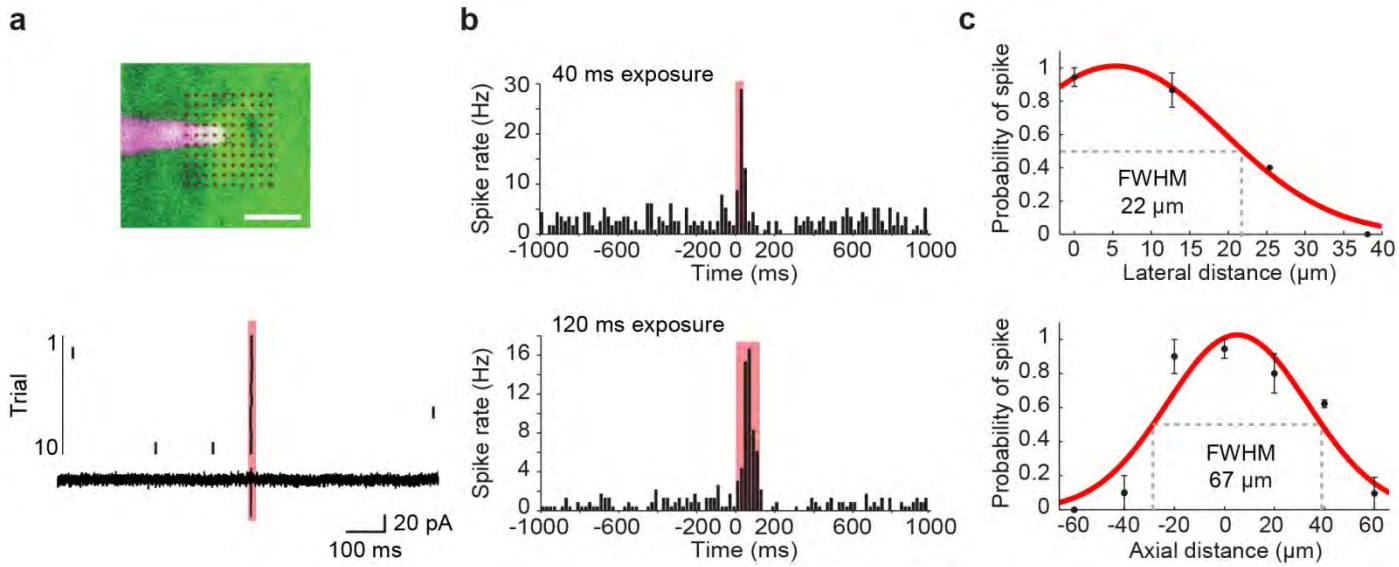

Supplementary Figure 3

Single cell two-photon raster photostimulation *in vivo*

(a) Top: Cell-attached patch clamp recording from a neuron in layer 2/3 of barrel cortex expressing C1V1-2A-YFP in vivo overlaid with the photostimulation pattern (pipette, magenta; YFP, green; photostimulation pattern, grid of red spots; scale bar, 10 µm.) Bottom: Raster of spike times around stimulus delivery over 10 trials, with the electrophysiological recording from trial 1. Note the time-locked precision and reliable response to photostimulation (red bar).

(b) Top: Raster of spike times around stimulus delivery for four neurons photostimulated for 40 ms. Bottom: Raster of spike times around stimulus delivery for nine neurons photostimulated for 120 ms.

(c) Lateral (top) and axial (bottom) resolution of photostimulated action potentials.

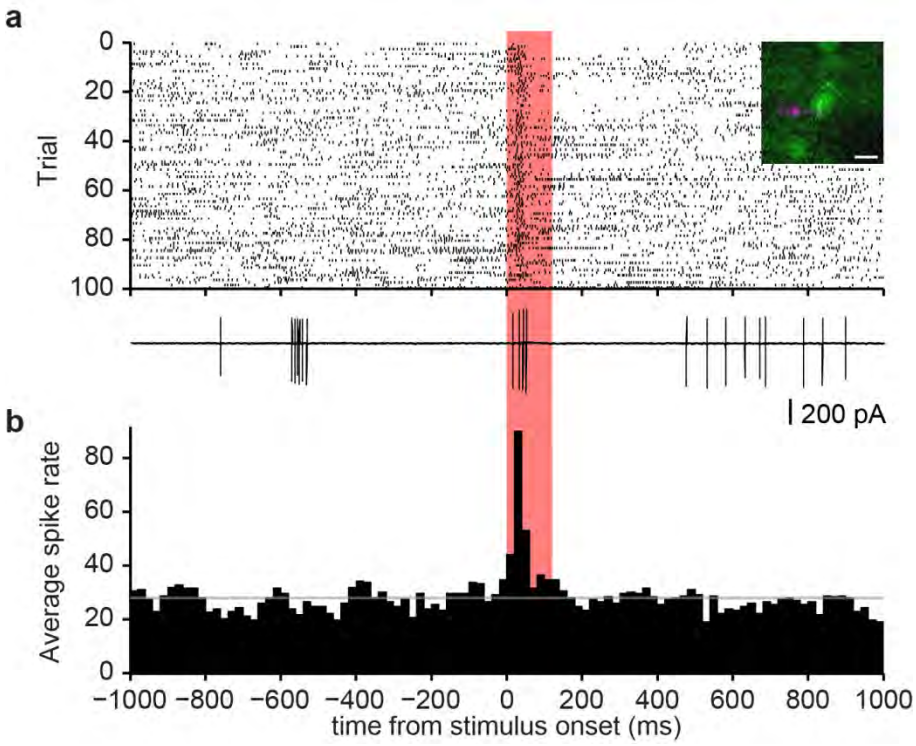

Supplementary Figure 4

Single cell two-photon raster photostimulation of an interneuron *in vivo*

(a) Photostimulation (120 ms grid, red bar) of a fast-spiking putative interneuron in layer 2/3 of barrel cortex in vivo (inset, two-photon targeted cell-attached patch clamp recording, scale bar 10 μm) revealed robust action potential generation despite ongoing spontaneous activity (raster).

(b) The average spike rate during photostimulation (red bar) increased sharply relative to the high background rate.

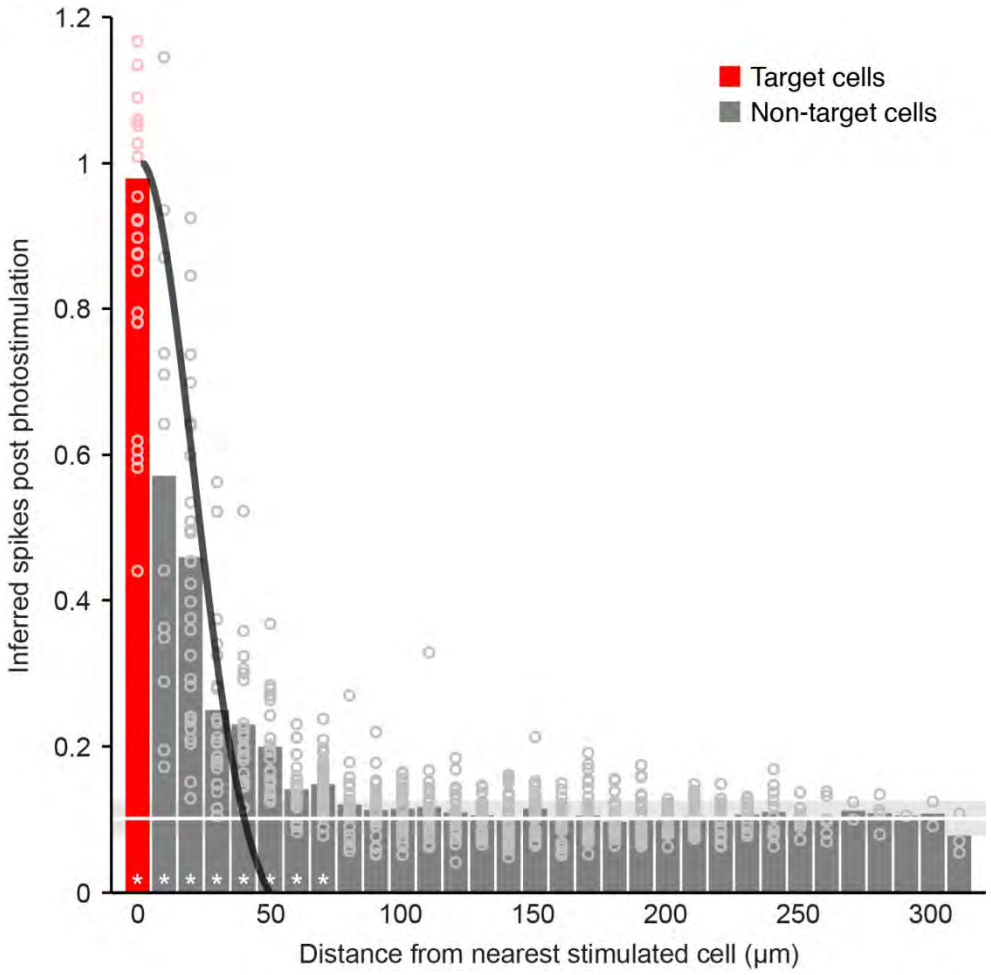

Supplementary Figure 5

Activation versus distance from nearest stimulated neuron during simultaneous activation of ten target neurons

Pooled data from multiple experiments where 10 neurons were photostimulated in layer 2/3 of barrel cortex, and the resulting activity was measured in the local network. Neurons are binned by distance from nearest stimulated neuron in 10 µm increments. The red bin at zero is comprised solely of the photostimulated neurons. Grey bins contain all non-stimulated neurons in the field of view. Open circles are individual neurons. The white line and shading indicates mean ± SD background firing rate across all non-stimulated neurons during non-stimulation periods. The curve defining the spatial resolution of single cell photostimulation from Supplementary Figure 3 is overlaid in black. Note that numerous cells at 50 µm or greater from the nearest stimulated cell are above the level of background spontaneous activity, which are not likely to have been directly photostimulated. White stars indicate significance of average spike count within a bin versus baseline (Mann-Whitney test $p < 0.05$ [Bonferroni corrected for 33 bins $p < 0.0003$]). n = 3 mice, one FOV and one 10-neuron stimulation pattern per mouse with 10 trials per repeat and ~14 repeats per mouse. Total of 672 imaged neurons, 30 of which were stimulated in 370 trials.

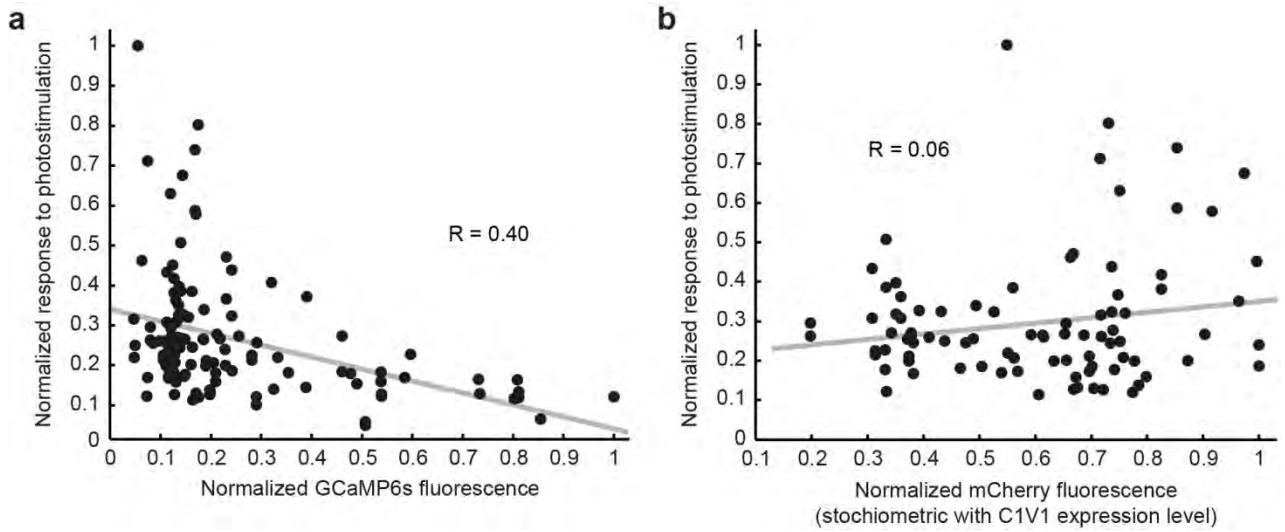

Supplementary Figure 6

Correlations of response to photostimulation with GCaMP6s and C1V1 expression levels

(a) Significant inverse relationship (Spearman rho = 0.40; $p < 0.0001$) between normalized response to photostimulation (sum of inferred spikes post-stimulation) and normalized GCaMP6s expression levels (mean brightness of region of interest containing neuron) indicates that the more strongly expressing neurons do not respond as well to the perturbation. Given the high reliability of the perturbation (Figs. 2 & 3), this is likely due to the known issue of GCaMP overexpression leading to aberrant physiology (Chen et al 2013, Tian et al 2009). The response to perturbation could thus be used to calibrate the dynamic range of the GCaMP6s signal per action potential in each neuron separately. These data are from experiments in which ten neurons were photostimulated simultaneously.

(b) There is a small but insignificant correlation (Spearman rho = 0.06, $p = 0.60$) between the normalized response to photostimulation and the normalized C1V1 expression level (as indicated by the mean brightness of mCherry, which is expressed in stoichiometric concentration due to the 2A peptide). These data are from experiments in which ten neurons were photostimulated simultaneously (not including the top 25% brightest GCaMP6s-expressing neurons based on a).

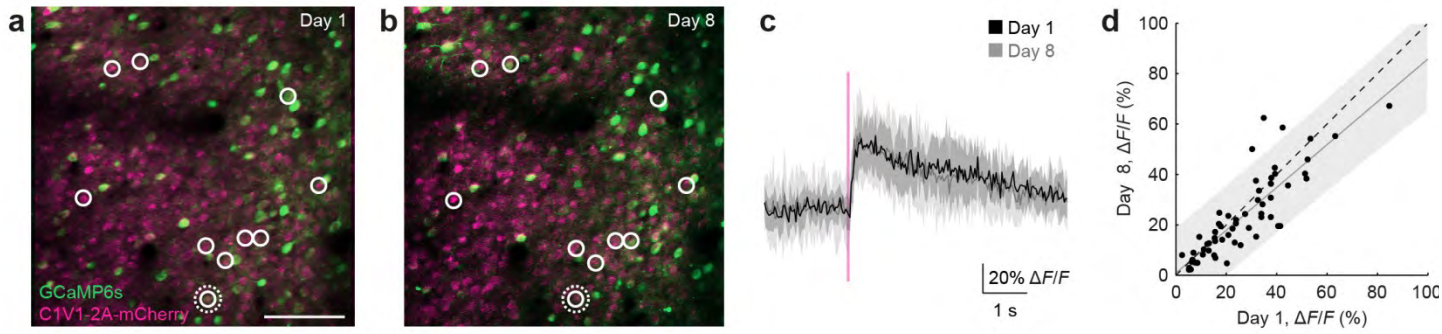

Supplementary Figure 7

Longitudinal stability of all-optical photostimulation and readout

(a) Imaging and selection of targets in layer 2/3 of somatosensory cortex on Day 1 of a representative experiment. White circles are the photostimulated targets (scale bar, 100 μm).

(b) The same field of view as (a), one week later.

(c) Mean ± SD calcium transient (for ten photostimulation trials) of the target cell in the dashed circle in (a) on day 1 (black) and day 8 (gray).

(d) Data from three fields of view showed the mean responses to photostimulation on day 1 and day 8 were highly correlated, implying the same responses could be observed from the same neurons one week apart. The dashed line is the unity line. The solid grey line indicates the fit with 95% confidence interval shaded in grey.

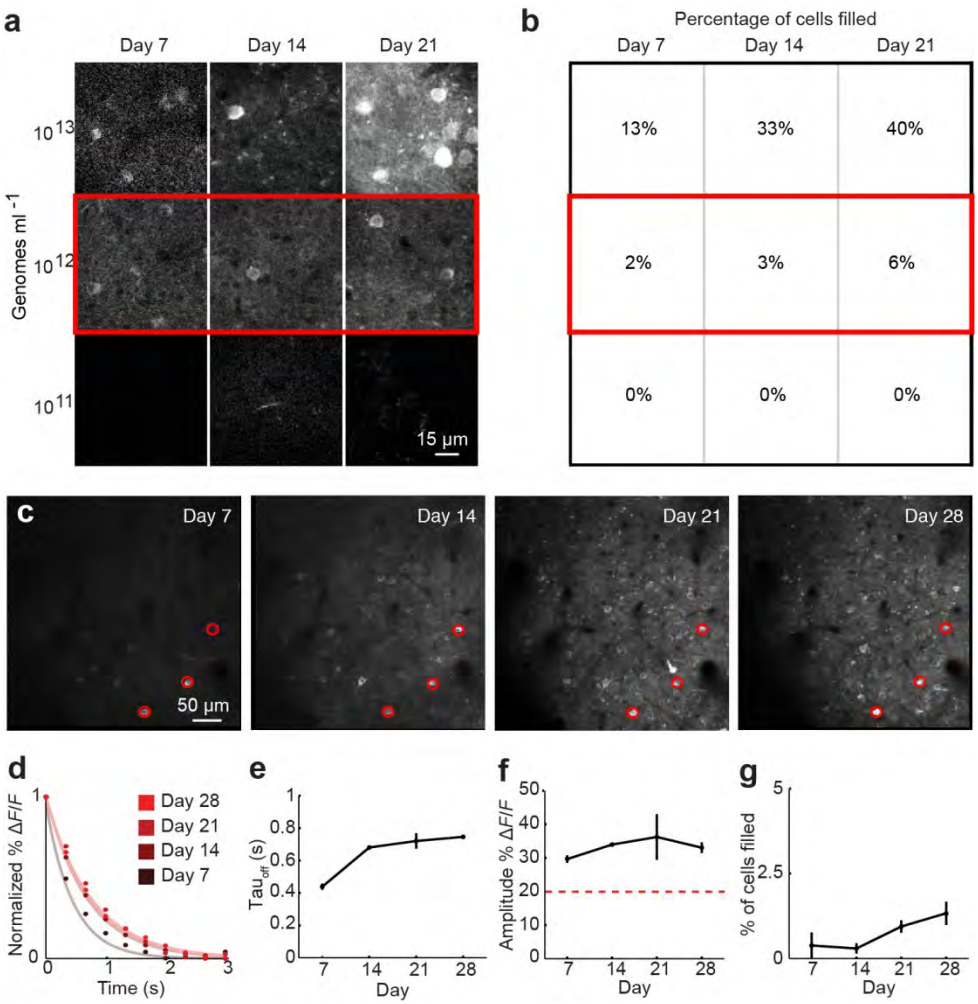

Supplementary Figure 8

Optimized GCaMP6s expression

(a) A narrow window of viral titer (rows) is crucial for sufficient and long-lasting expression over time (columns). Note lack of expression with titer that is too low (bottom row) and brightly-filled neurons with titer that is too high (top row).

(b) Quantification of the percentage of brightly-filled cells in depth-matched (~160 µm deep) fields of view at titers and time-points corresponding to the rows and columns in (a) from acute craniotomy preparations. Data from 11 mice.

(c) Example cell-matched fields of view from a chronic window preparation at 4 time-points post-injection using the 10^{12} genomes ml-1 titer highlighted in red in (a) and (b). Note example cells identified across 4 weeks highlighted in red.

(d) Monoexponential fit (curves) to cell-matched calcium transient decays (points) recorded at each time point (see figure key) during spontaneous activity under 0.5% isofluorane anesthesia. Transients were identified following a threshold crossing of 20% above the median value of each cell's dF/F trace. They were then normalised to the peak following this crossing. n = 2 animals (1323 cells total)

(e) Quantification of the change with time of the decay time constant (Tau_{off}) of the monoexponential fits shown in (d).

(f) Amplitude of cell-matched calcium transients measured at each time point. Transient threshold is shown as dotted red line.

(g) Percentage of brightly-filled neurons in analysed fields of view at each time point.

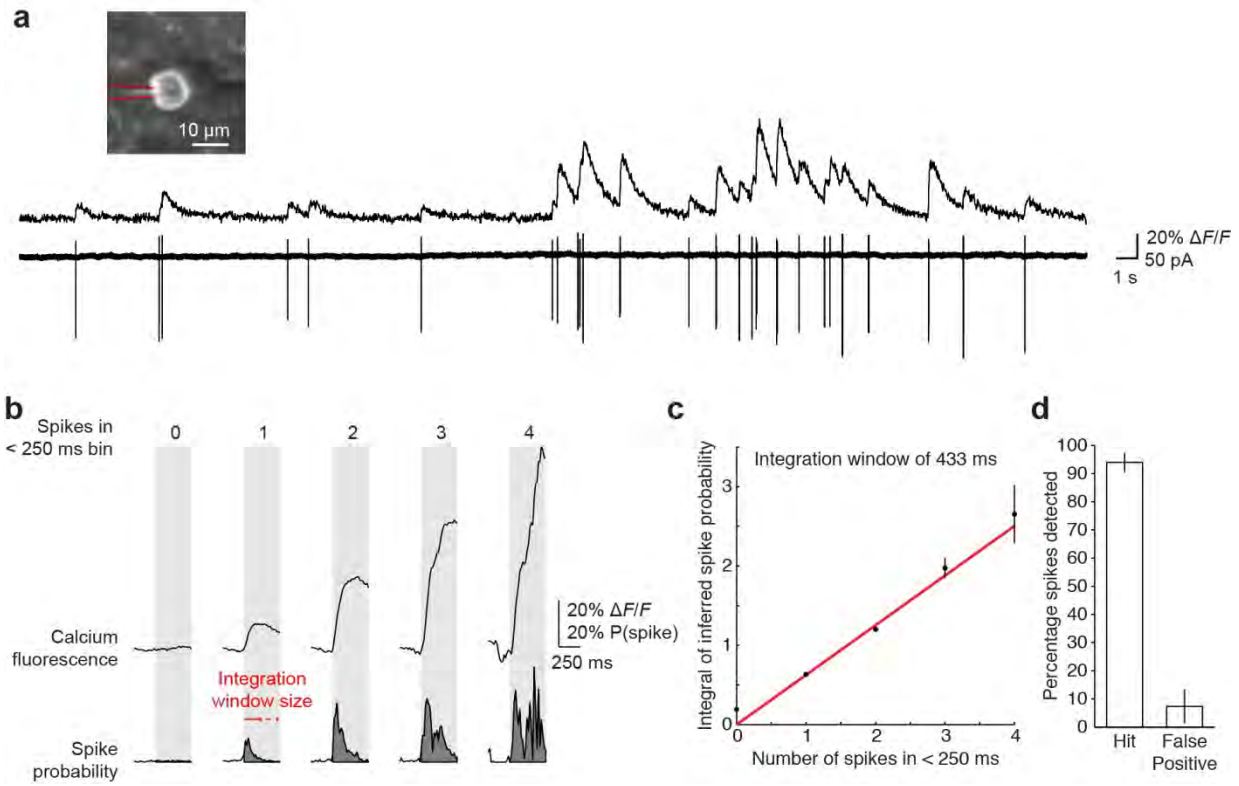

Supplementary Figure 9

Sensitivity of spike readout

(a) Confirmation of single action potential resolution in a GCaMP6s-expressing neuron obtained during two-photon targeted cell-attached patch clamp recording while imaging at 60 Hz.

(b) The calcium rise recorded from this example neuron in response to one or more action potentials shows the characteristic amplitude and time course of GCaMP6s (top traces). The inferred action potential probability from the deconvolution algorithm indicates the likelihood of a spike somewhat smeared over time.

(c) Integrating the inference over a time-window of 433 ms results in a high coefficient of determination (R2 = 0.54) of the linear fit (y = 0.63x + 0) between inferred probability of spiking and actual spiking recorded in cell-attached configuration. 433 ms resulted in a better fit versus other durations between 100 and 1000 ms. n = 4 neurons. SEM across all 250 ms epochs containing a reported number of spikes: 0 spikes n = 141; 1 spike n = 332; 2 spikes n = 236; 3 spikes n = 64; 4 spikes n = 6.

(d) Analysis confirming the ability of GCaMP6s to reliably report single spikes, based on Chen et al 2013. Hit rate and false positive rate for identification of single isolated spikes was calculated by using a template and threshold of correlation as determined using the neuron in (a). Total of 266 single spikes and 45 no spike periods from 3 neurons, not including neuron (a).